CHEMISTRY

Oxygen-deficient metal oxides supported nano-intermetallic $InNi_3C_{0.5}$ toward efficient CO_2 hydrogenation to methanol

Chao Meng[1], Guofeng Zhao[1]*, Xue-Rong Shi[2,3]*, Pengjing Chen[1], Ye Liu[1], Yong Lu[1]*

Direct CO_2 hydrogenation to methanol using renewable energy–generated hydrogen is attracting intensive attention, but qualifying catalysts represents a grand challenge. Pure-/multi-metallic systems used for this task usually have low catalytic activity. Here, we tailored a highly active and selective $InNi_3C_{0.5}/ZrO_2$ catalyst by tuning the performance-relevant electronic metal-support interaction (EMSI), which is tightly linked with the ZrO_2 type–dependent oxygen deficiency. Highly oxygen-deficient monoclinic-ZrO_2 support imparts high electron density to $InNi_3C_{0.5}$ because of the considerably enhanced EMSI, thereby enabling $InNi_3C_{0.5}$/monoclinic-ZrO_2 with an intrinsic activity three or two times as high as that of $InNi_3C_{0.5}$/amorphous-ZrO_2 or $InNi_3C_{0.5}$/tetragonal-ZrO_2. The EMSI-governed catalysis observed in the $InNi_3C_{0.5}/ZrO_2$ system is extendable to other oxygen-deficient metal oxides, in particular $InNi_3C_{0.5}/Fe_3O_4$, achieving 25.7% CO_2 conversion with 90.2% methanol selectivity at 325°C, 6.0 MPa, 36,000 ml g_{cat}^{-1} $hour^{-1}$, and H_2/CO_2 = 10:1. This affordable catalyst is stable for at least 500 hours and is also highly resistant to sulfur poisoning.

INTRODUCTION

The rapid growth of carbon-based energy consumption along with the global economic development are responsible for a massive emission of carbon dioxide (CO_2), raising its atmospheric concentration from suitable 300 up to 415 ppmv (parts per million by volume) in the last 60 years and causing serious problems of global warming, glacier melting, and ocean acidification (*1*). CO_2 capture and storage technology potentially reduces this emission, but the high storage cost and uncertainty about CO_2 leakage greatly limit the application of this technology, while converting CO_2 into commodity chemicals is a promising approach to recycle massive quantities of CO_2 (*2*–*5*). Among the commodity chemicals, methanol is not only a clean alternative fuel for gasoline and diesel but also an excellent chemical platform to produce olefins and other high value-added chemicals commonly obtained from crude oil, with a worldwide demand of ~50 million tons per year (*6*, *7*). In this context, the catalytic hydrogenation of CO_2 to methanol (denoted as CO_2-to-methanol) using renewable hydrogen (H_2, produced by solar energy, hydropower, and wind power) has been attracting great attention for a CO_2 circular economy (*8*). Moreover, this reversible reaction also shows substantial potential to be used as a H_2 storage distribution system for applications in H_2-O_2 fuel cells (*9*). However, this is a grand challenge because of the chemical inertness of the CO_2 molecule (*5*, *10*). Accordingly, substantial catalytic advances are urgently required for the large-scale hydrogenation of CO_2 to methanol.

Over the past decades, photo- and electro-catalytic CO_2 hydrogenation to methanol has been greatly advanced but still suffers from low productivity originating from the low photo-/electro-energy density (*4*, *11*). A variety of homogeneous complexes enables a high methanol yield under relatively mild conditions (*12*), but their practical applications are limited by their high prices and complicated operations. Heterogeneous catalysts are composed of active components loaded on solid supports, endowed with the superior ability to address the operation issues. Nano-copper catalysts supported on metal oxides were extensively studied (*5*, *10*, *13*, *14*), but severe problems exist, including low methanol selectivity (usually below 60%) caused by the competing reverse water-gas shift (RWGS) reaction and rapid deactivation by Cu sintering (*15*). A range of precious metal catalysts, such as Pd/In_2O_3 (*16*) and $Au/ZnO(CeO_x/TiO_2)$ (*17*, *18*), were successfully used as a replacement of copper but are compromised by their limited natural abundance. A series of bimetallic oxides were found to be promising for this reaction, such as 5% CO_2 conversion, 99.8% methanol selectivity, and 0.295 g_{MeOH} g_{cat}^{-1} $hour^{-1}$ methanol productivity on In_2O_3/ZrO_2 (*19*), and 10% CO_2 conversion, 86% methanol selectivity, and 0.73 g_{MeOH} g_{cat}^{-1} $hour^{-1}$ methanol productivity on ZnO-ZrO_2 (*20*). Recently, Nørskov and coworkers (*21*) discovered a Ni_5Ga_3 intermetallic catalyst with the aid of theoretical calculations, achieving CO_2 conversion of 4.9%, methanol selectivity of 44.8%, and methanol productivity of 0.1 g_{MeOH} g_{cat}^{-1} $hour^{-1}$ at atmospheric pressure. García-Trenco *et al.* (*22*) unveiled a PdIn catalyst, exhibiting CO_2 conversion of 0.6%, methanol selectivity of above 80%, and methanol productivity of 0.13 g_{MeOH} g_{cat}^{-1} $hour^{-1}$. Despite the fact that no intermetallics have proved to be superior over the catalysts reported ever, it is worthy to explore these emerging catalyst candidates for CO_2 hydrogenation, because the intermetallic compounds have facilely tunable components, variable constructions, and reconfigurable electronic structures, and great progress has been made on nano-intermetallic catalysts for CO_2 hydrogenation to methanol.

Very recently, the nano-intermetallic compound $InNi_3C_{0.5}$ structured on an Al_2O_3/Al-fiber, with superior RWGS performance at and above 400°C, was also found to be highly selective for the CO_2-to-methanol reaction below 300°C but not active enough (*23*). Notably, the electronic metal-support interaction (EMSI) is paramount to improve the catalyst performance via tuning the electronic

[1]Shanghai Key Laboratory of Green Chemistry and Chemical Processes, School of Chemistry and Molecular Engineering, East China Normal University, Shanghai 200062, China. [2]Department of Materials Engineering, Shanghai University of Engineering Science, Shanghai 201620, China. [3]Institute of Physical Chemistry, University of Innsbruck, Innrain 80-82, Innsbruck, Austria.
*Corresponding author. Email: gfzhao@chem.ecnu.edu.cn (G.Z.); shixuer05@mails.ucas.ac.cn (X.-R.S.); ylu@chem.ecnu.edu.cn (Y. Lu)

properties of metal nanoparticles by supports (*24*–*26*). Campbell (*24*) showed that small platinum clusters experience large electronic perturbation when in contact with ceria, strongly enhancing the catalytic performance for the water-gas shift reaction. Recently, Rodriguez *et al.* (*27*) reported the advantages of metal-oxide and metal-carbide interfaces for CO_2 conversion to methanol and confirmed that the metal-support interactions modify the electronic properties of metals. Moreover, it is interesting to recognize that zirconia (ZrO_2) with oxygen vacancies traps electrons at vacancy centers and modulates the electronic states of as-anchored metal nanoparticles (*28*, *29*). For instance, Ni *et al.* (*29*) successfully tuned the electron density of Ni particles by ZrO_2 with oxygen vacancies to enhance the hydrogenation of fatty acids to alcohols. These findings may give an interesting hint to develop a high-performance CO_2-to-methanol catalyst by dispersing $InNi_3C_{0.5}$ nanoparticles onto reducible oxides that can generate abundant oxygen vacancies. To check this idea, we chose three ZrO_2 supports that can generate different amounts of oxygen vacancies, including monoclinic-ZrO_2 (*m*-ZrO_2), tetragonal-ZrO_2 (*t*-ZrO_2), and amorphous-ZrO_2 (*a*-ZrO_2), to tailor the catalysts. Among them, $InNi_3C_{0.5}$/*m*-ZrO_2 shows an excellent performance with 11.2% CO_2 conversion and 85.4% methanol selectivity under the typical reaction conditions. A combined study of spectroscopic and electron microscopic methods, and theoretical calculations confirms that the electron structure of $InNi_3C_{0.5}$ is tuned by ZrO_2 (especially by *m*-ZrO_2 with abundant oxygen vacancies), accompanied by the gradually enhanced CO_2 activation on the $InNi_3C_{0.5}$ surface, thereby leading to remarkable improvement of the CO_2 conversion to methanol. According to this inspiring clue, a more efficient and affordable $InNi_3C_{0.5}/Fe_3O_4$ catalyst, with further enhanced EMSI between $InNi_3C_{0.5}$ and Fe_3O_4, was tailored by carburizing a In_2O_3-NiO/Fe_2O_3 precursor. This catalyst achieves 25.7% CO_2 single-pass conversion and 90.2% methanol selectivity at 325°C, gas hourly space velocity (GHSV) of 36,000 ml g_{cat}^{-1} $hour^{-1}$, H_2/CO_2 molar ratio of 10:1, and 6.0 MPa [or a high space time yield (STY) of 2.62 g_{MeOH} g_{cat}^{-1} $hour^{-1}$ with 18.8% conversion and 92.8% selectivity using a high GHSV of 115,500 ml g_{cat}^{-1} $hour^{-1}$]. Moreover, this catalyst shows high resistance to sulfur poisoning. We take a big step forward in tailoring of a stable and highly active/selective catalyst for efficient synthesis of methanol from CO_2 hydrogenation.

RESULTS

Structural, morphological, and textural features of $InNi_3C_{0.5}/ZrO_2$ catalysts

We initially loaded $InNi_3C_{0.5}$ on *m*-, *t*-, and *a*-ZrO_2 supports via incipient wetness impregnation and subsequent carburization (details in Materials and Methods). These catalysts were probed by x-ray diffraction (XRD), clearly identifying the characteristic patterns of $InNi_3C_{0.5}$ (PDF#28-0468), *m*-ZrO_2 (PDF#86-1449), and *t*-ZrO_2 (PDF#50-1089) (Fig. 1A). *a*-ZrO_2 in $InNi_3C_{0.5}$/*a*-ZrO_2 was partially transformed into *t*-ZrO_2 during the carburization process at 600°C, as the tetragonal phase is thermodynamically more stable than the amorphous phase at high temperature (*30*). The main diffraction peaks of $InNi_3C_{0.5}$ at 41.3° and 48.1° in these catalysts are similarly sharp and strong, indicating comparable grain size and crystallinity of $InNi_3C_{0.5}$. The transmission electron microscopy (TEM) images illustrate that these three catalysts exhibit a uniform dispersion of $InNi_3C_{0.5}$ grains with an average size of 16.0 ± 0.5 nm (Fig. 1, B to D). Moreover, the high-resolution TEM images (Fig. 1, E to G) show the lattice fringes of $InNi_3C_{0.5}$ (1-10) with spacing of 0.267 nm, indicating that the dominant exposed facet of $InNi_3C_{0.5}$ is the (111) plane (see detailed results and analysis in figs. S1 and S2). These three catalysts show rough and porous surface morphology aggregated from irregular-shaped lumps of 300 to 500 nm (fig. S3) and mesoporous feature with dominant mesopore size centered at 10 to 20 nm (fig. S4). The $InNi_3C_{0.5}$/*t*-ZrO_2 catalyst presents the largest specific surface area (SSA) of 52.0 m^2 g^{-1} (table S1), followed by $InNi_3C_{0.5}$/*m*-ZrO_2 (10.0 m^2 g^{-1}) and $InNi_3C_{0.5}$/*a*-ZrO_2 (5.0 m^2 g^{-1}).

Dependence of catalytic performance on ZrO_2 type

The $InNi_3C_{0.5}/ZrO_2$ catalysts were comparatively investigated for methanol synthesis from CO_2 hydrogenation in a continuous-flow fixed-bed tubular reactor, under the reaction conditions of 300°C, 4.0 MPa, H_2/CO_2 molar ratio of 3:1, and GHSV of 12,000 ml g_{cat}^{-1} $hour^{-1}$ (optimized as shown in fig. S5). The $InNi_3C_{0.5}/SiO_2$ catalyst offered a high methanol selectivity of 90% but a very low CO_2 conversion of only 2.5% (Fig. 2A; much lower than the thermodynamic equilibrium conversion of 11.6%; fig. S6). Our $InNi_3C_{0.5}/ZrO_2$ catalysts all raised CO_2 conversion markedly compared to $InNi_3C_{0.5}/SiO_2$, but interestingly, their catalytic performance showed a remarkable ZrO_2-type dependence. Only $InNi_3C_{0.5}$/*m*-ZrO_2 can achieve a CO_2 conversion (11.2%) close to thermodynamic equilibrium with an acceptable methanol selectivity of 85.4%. $InNi_3C_{0.5}$/*t*-ZrO_2 and $InNi_3C_{0.5}$/*a*-ZrO_2 delivered moderate conversions of 3.5 to 5.0% with similar methanol selectivity of 85 to 90%. As references, the pure ZrO_2 and SiO_2 supports were also tested in this reaction but yielded no more than 0.7% CO_2 conversion (Fig. 2A and table S2). Moreover, the STY of methanol was calculated to further assess the catalytic performance of the ZrO_2-supported $InNi_3C_{0.5}$ catalysts. $InNi_3C_{0.5}$/*m*-ZrO_2 exhibited a high STY of 0.62 g_{MeOH} g_{cat}^{-1} $hour^{-1}$ at 300°C, much higher than that of $InNi_3C_{0.5}$/*t*-ZrO_2 (0.30 g_{MeOH} g_{cat}^{-1} $hour^{-1}$), $InNi_3C_{0.5}$/*a*-ZrO_2 (0.20 g_{MeOH} g_{cat}^{-1} $hour^{-1}$), and $InNi_3C_{0.5}/SiO_2$ (0.18 g_{MeOH} g_{cat}^{-1} $hour^{-1}$) (Fig. 2B and table S3), as well as most reported catalysts (table S4).

These catalysts have similar surface morphology (aggregation of irregular shaped lumps; fig. S3) and $InNi_3C_{0.5}$ grain size (~16 nm; Fig. 1, B to D), excluding the responsibility for their discrepancy of activity for CO_2 hydrogenation. To assess the intrinsic activity, their turnover frequencies (TOFs; defined as the number of reactant consumed on an active site per unit time) were measured. Not surprisingly, $InNi_3C_{0.5}$/*m*-ZrO_2 offered the highest TOF of 72.2 $hour^{-1}$ (Fig. 2B and table S3), being three and two times as high as that of $InNi_3C_{0.5}$/*a*-ZrO_2 (23.8 $hour^{-1}$) and $InNi_3C_{0.5}$/*t*-ZrO_2 (34.2 $hour^{-1}$). Apparently, a special EMSI between ZrO_2 and $InNi_3C_{0.5}$ is generated and accounts for the improvement of the catalyst activity, while the EMSI shows strong ZrO_2-type dependence. However, the nature of this ZrO_2-type dependence of the catalytic performance-relevant EMSI is still not clear.

Oxygen vacancy relevant EMSI

The EMSI between $InNi_3C_{0.5}$ and ZrO_2 supports was first explored by the quasi–in situ x-ray photoelectron spectroscopy (XPS) technique, with the spectra displayed in Fig. 3. For the $InNi_3C_{0.5}/SiO_2$ catalyst, the binding energies of Ni $2p_{3/2}$ and Ni $2p_{1/2}$ located at 852.7 and 870.1 eV (Fig. 3A) are equal to those of the pure Ni^0 metal. By comparison, the binding energy of Ni $2p_{3/2}$ for $InNi_3C_{0.5}$/*a*-ZrO_2, $InNi_3C_{0.5}$/*t*-ZrO_2, and $InNi_3C_{0.5}$/*m*-ZrO_2 is respectively lowered

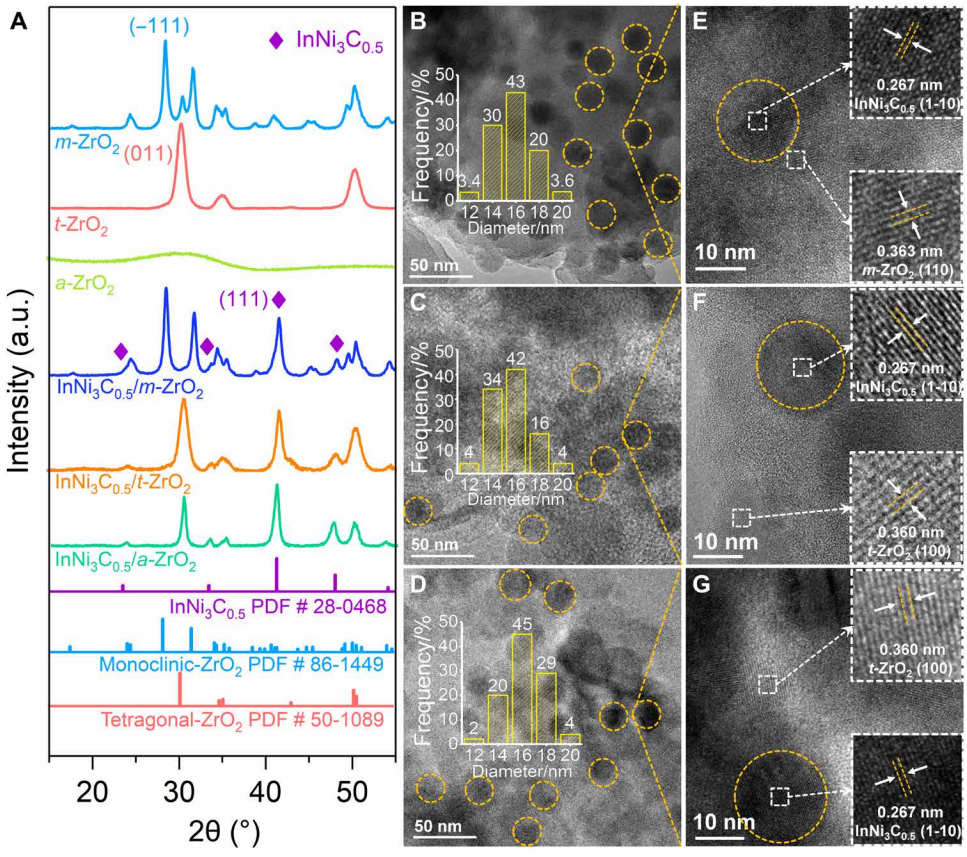

Fig. 1. Structures of ZrO_2 supports and corresponding catalysts. (**A**) XRD patterns of *m*-ZrO_2, *t*-ZrO_2, *a*-ZrO_2, $InNi_3C_{0.5}$/*m*-ZrO_2, $InNi_3C_{0.5}$/*t*-ZrO_2, and $InNi_3C_{0.5}$/*a*-ZrO_2. TEM images of (**B**) $InNi_3C_{0.5}$/*m*-ZrO_2, (**C**) $InNi_3C_{0.5}$/*t*-ZrO_2, and (**D**) $InNi_3C_{0.5}$/*a*-ZrO_2 (insets: corresponding size distribution of the $InNi_3C_{0.5}$ nanoparticles). a.u., arbitrary units. High-resolution TEM images of a typical $InNi_3C_{0.5}$ nanoparticle supported on (**E**) *m*-ZrO_2, (**F**) *t*-ZrO_2, and (**G**) *a*-ZrO_2 [insets: lattice fringes with distance of 0.267 nm corresponding to the $InNi_3C_{0.5}$ (1-10) crystal plane, 0.363 nm to the *m*-ZrO_2 (110) crystal plane, and 0.360 nm to the *t*-ZrO_2 (100) crystal plane].

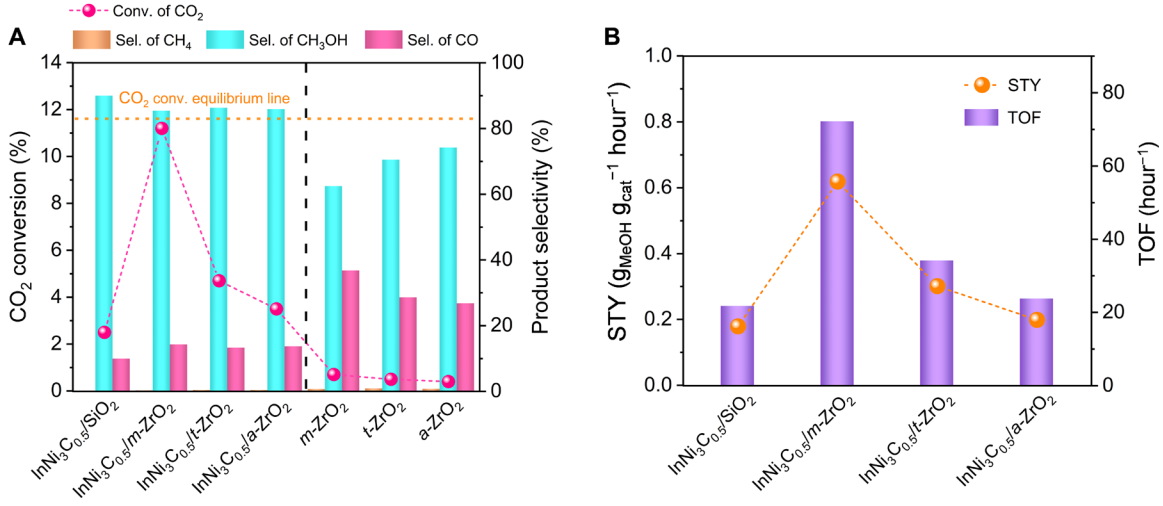

Fig. 2. Catalytic performance of various catalysts. (**A**) CO_2 conversion and product selectivity (300°C, 4.0 MPa, $H_2/CO_2 = 3:1$, and a GHSV of 12,000 ml g_{cat}^{-1} $hour^{-1}$). (**B**) STY of methanol and TOF (300°C, 4.0 MPa, $H_2/CO_2 = 3:1$, and a GHSV of 24,000 ml g_{cat}^{-1} $hour^{-1}$).

from 852.7 to 852.5, 852.4, and 852.1 eV, showing the gradually enriched electron density especially of *m*-ZrO_2–supported $InNi_3C_{0.5}$. Similarly, the electron enrichment in In and C elements is also observed on $InNi_3C_{0.5}$/*t*-ZrO_2 and especially $InNi_3C_{0.5}$/*m*-ZrO_2 (Fig. 3B and fig. S7): For example, the binding energy of In $3d_{5/2}$ (*31*) shifts from 443.6 eV (for $InNi_3C_{0.5}/SiO_2$ and $InNi_3C_{0.5}$/*a*-ZrO_2) to 443.3 (for $InNi_3C_{0.5}$/*t*-ZrO_2) and 443.2 eV (for $InNi_3C_{0.5}$/*m*-ZrO_2). The above results confirm the existence of the ZrO_2 type–dependent

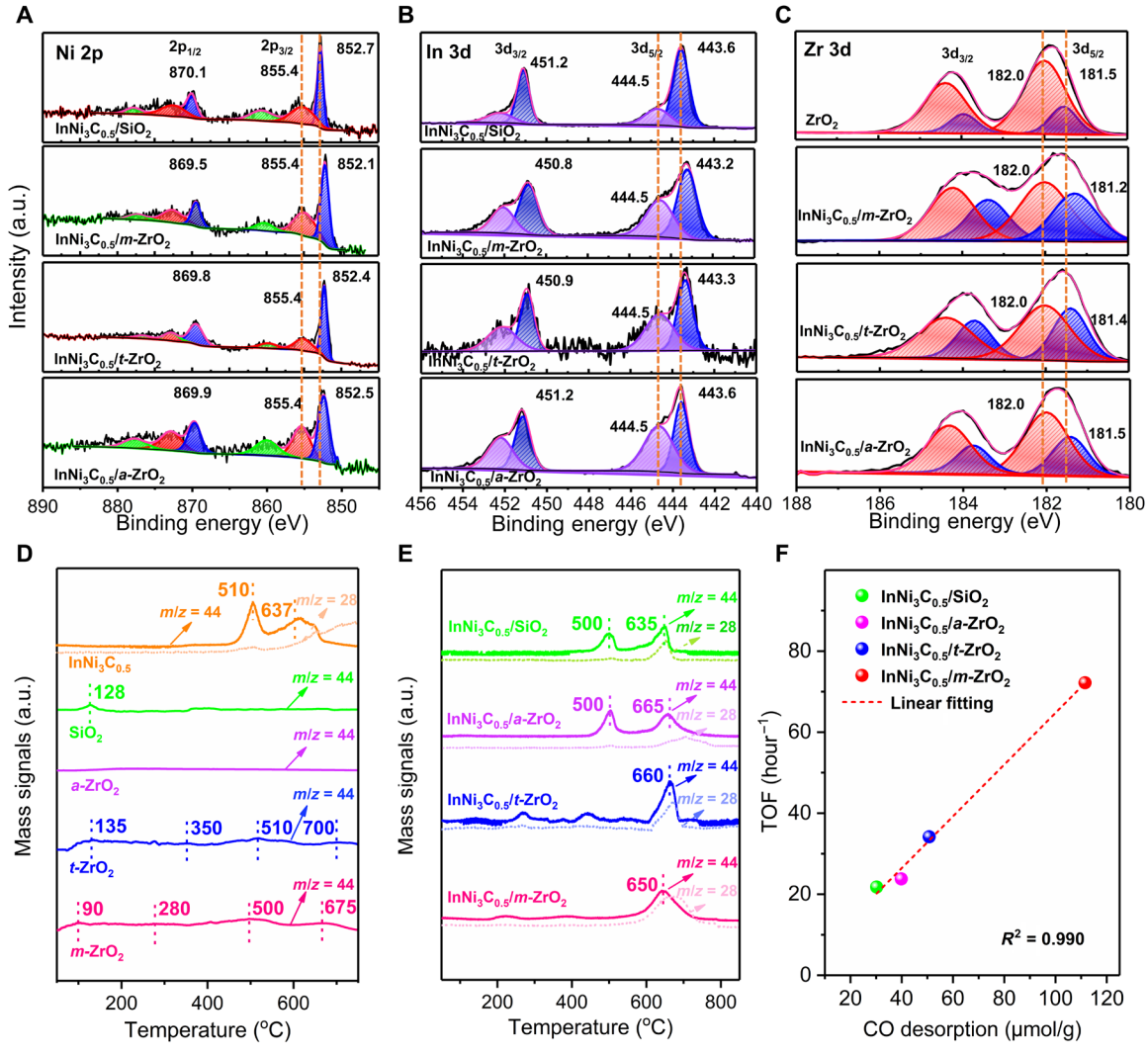

Fig. 3. Electronic states and ability to activate CO_2 of ZrO_2 supports and corresponding catalysts. XPS spectra in (**A**) Ni 2p and (**B**) In 3d regions of $InNi_3C_{0.5}/SiO_2$, $InNi_3C_{0.5}/m\text{-}ZrO_2$, $InNi_3C_{0.5}/t\text{-}ZrO_2$, and $InNi_3C_{0.5}/a\text{-}ZrO_2$. XPS spectra in (**C**) Zr 3d region for $a\text{-}ZrO_2$ (as the reference), $InNi_3C_{0.5}/m\text{-}ZrO_2$, $InNi_3C_{0.5}/t\text{-}ZrO_2$, and $InNi_3C_{0.5}/a\text{-}ZrO_2$, and analysis fittings in table S5. (**D**) CO_2-TPD-MS profiles for unsupported $InNi_3C_{0.5}$ nano-intermetallic, pure SiO_2, $a\text{-}ZrO_2$, $t\text{-}ZrO_2$, and $m\text{-}ZrO_2$ supports. (**E**) CO_2-TPD-MS profiles for $InNi_3C_{0.5}/SiO_2$, $InNi_3C_{0.5}/a\text{-}ZrO_2$, $InNi_3C_{0.5}/t\text{-}ZrO_2$, and $InNi_3C_{0.5}/m\text{-}ZrO_2$ catalysts. MS signal of the carbonaceous species for CO_2 desorption: CO_2 signal [mass/charge ratio (m/z) = 44] and CO signal (m/z = 28). (**F**) Plot of the TOF as a function of the amount of CO desorption (reaction conditions for TOF measurements: 300°C, 4.0 MPa, H_2/CO_2 = 3:1, and GHSV = 24,000 ml g_{cat}^{-1} $hour^{-1}$).

EMSI and indicate that the strongest EMSI takes place between $InNi_3C_{0.5}$ and $m\text{-}ZrO_2$. It should be noticed that some Ni^{2+} (at 855.4 eV) and In^{3+} (at 444.5 eV) species are observed on all ZrO_2-supported $InNi_3C_{0.5}$ catalysts (Fig. 3, A and B), which are likely from the dissolving of Ni^{2+} and In^{3+} ions into the ZrO_2 lattice (*29*, *32*). In addition, the peak areas of the XPS spectra of surface Ni^{2+} and In^{3+} species in all ZrO_2-supported $InNi_3C_{0.5}$ catalysts are almost identical, and therefore, we believe that the Ni^{2+} and In^{3+} species are not responsible for the discrepancy of their activity for CO_2 hydrogenation.

The XPS spectrum of Zr $3d_{5/2}$ in pure $a\text{-}ZrO_2$ can be deconvoluted into two peaks with binding energies of 181.5 and 182.0 eV (Fig. 3C), respectively, assigned to partially reduced $Zr^{\delta+}$ (denoted as Zr_I, $\delta < 4$; related to oxygen vacancy) and stoichiometric ZrO_2 (Zr_{II}, Zr^{4+}) (*33*). In comparison with pure $a\text{-}ZrO_2$, the three catalysts have more Zr_I species while showing lowered binding energy of Zr $3d_{5/2}$ from 181.5 eV to 181.2 to 181.4 eV (Fig. 3C). $InNi_3C_{0.5}/m\text{-}ZrO_2$ has the highest amount of Zr_I species (i.e., oxygen vacancies) and the lowest binding energy of Zr $3d_{5/2}$ (i.e., enriched electron density), followed by $InNi_3C_{0.5}/t\text{-}ZrO_2$ and then $InNi_3C_{0.5}/a\text{-}ZrO_2$ (table S5 and figs. S8 and S9). This sequence is in accord with the electron density tendency of $InNi_3C_{0.5}/m\text{-}ZrO_2$ > $InNi_3C_{0.5}/t\text{-}ZrO_2$ > $InNi_3C_{0.5}/a\text{-}ZrO_2$ (Fig. 3, A and B, and fig. S7). We are thus confident that the EMSI is gradually enhanced with the increase in Zr_I species (i.e., oxygen vacancies) of the ZrO_2 supports, which accounts for the ZrO_2 type–dependent EMSI and the improvement of CO_2 hydrogenation activity especially of the $InNi_3C_{0.5}/m\text{-}ZrO_2$ catalyst.

To further confirm this oxygen vacancy relevant EMSI and the dependence of EMSI strength on ZrO_2 type, these three catalysts were further investigated using hydrogen temperature-programmed desorption (TPD), electron paramagnetic resonance (EPR), and in

situ diffuse reflectance infrared Fourier transform spectroscopy (DRIFTS) of CO adsorption, with the results shown in fig. S10. All catalysts offer one H_2 desorption peak at 110°C (fig. S10A), which is ascribed to the H-species adsorbed on the $InNi_3C_{0.5}$ surface. The area of this peak is almost identical for these catalysts, in line with their same particle size and amount of $InNi_3C_{0.5}$, but $InNi_3C_{0.5}/m\text{-}ZrO_2$ shows a narrower peak than the other two catalysts, suggesting a quite uniform electron structure of $InNi_3C_{0.5}$ surface in comparison with the other two (*34*). Most notably, a strong H_2 desorption peak appears at 620°C for $InNi_3C_{0.5}/m\text{-}ZrO_2$, attributed to the H anions ($H^{\delta-}$) held at coordinatively unsaturated Zr_I sites (*29*, *35*), but a very weak peak at 576°C for $InNi_3C_{0.5}/t\text{-}ZrO_2$ even nothing (at 550° to 650°C) for $InNi_3C_{0.5}/a\text{-}ZrO_2$. As generally acknowledged, the surface of some reducible oxides (e.g., CeO_2, TiO_2, and ZrO_2) can be partially reduced by H_2 in association with the oxygen vacancy formed (*36*), and the as-formed oxygen vacancies are negatively charged with electron density maximally localized at the vacancy center (*28*). Clearly, the amount of $H^{\delta-}$ on Zr_I sites (i.e., oxygen vacancies) follows the order $InNi_3C_{0.5}/m\text{-}ZrO_2$ > $InNi_3C_{0.5}/t\text{-}ZrO_2$ > $InNi_3C_{0.5}/a\text{-}ZrO_2$ (fig. S10A). Moreover, the EPR spectra of these three $InNi_3C_{0.5}/ZrO_2$ catalysts show axial signals with *g* value of 2.003 (fig. S10B), further indicating the presence of oxygen vacancies (*37*). As expected, the signal intensity of $InNi_3C_{0.5}/m\text{-}ZrO_2$ is much higher than that of $InNi_3C_{0.5}/t\text{-}ZrO_2$ and followed by $InNi_3C_{0.5}/a\text{-}ZrO_2$. Undoubtedly, $InNi_3C_{0.5}/m\text{-}ZrO_2$ has a much higher density of oxygen vacancies than the other two, in good agreement with our XPS results (table S5 and figs. S8 and S9) and literature results (*29*). In addition, as shown in fig. S10C, linearly adsorbed CO with infrared band at 2077 cm^{-1} (*23*) is detected on $InNi_3C_{0.5}/SiO_2$ at room temperature. This linear adsorption of CO is also observed on the $InNi_3C_{0.5}/ZrO_2$ catalysts but exhibits a visible red shift from 2077 to 2075 ($InNi_3C_{0.5}/a\text{-}ZrO_2$) and further to 2047 and 2046 cm^{-1} ($InNi_3C_{0.5}/t\text{-}ZrO_2$ and $InNi_3C_{0.5}/m\text{-}ZrO_2$, respectively) because of an enhanced electron back-donation from $InNi_3C_{0.5}$ to the anti-bonding orbitals of CO (*38*). These results confirm again the EMSI-enhanced electron density of $InNi_3C_{0.5}$, which is improved according to the oxygen vacancy density that is dependent on ZrO_2 type.

CO_2 adsorption and activation

Effective adsorption and activation of CO_2 on the catalyst is the prerequisite for converting CO_2 to methanol. Therefore, CO_2-TPD experiments in combination with mass spectrometry (MS) were conducted for the catalysts ($InNi_3C_{0.5}/m\text{-}ZrO_2$, $InNi_3C_{0.5}/t\text{-}ZrO_2$, $InNi_3C_{0.5}/a\text{-}ZrO_2$, and $InNi_3C_{0.5}/SiO_2$) as well as for the pure supports (SiO_2, *m*-ZrO_2, *t*-ZrO_2, and *a*-ZrO_2) and unsupported $InNi_3C_{0.5}$ as references. The supports desorb little CO_2, showing the poor ability to adsorb CO_2, while the unsupported $InNi_3C_{0.5}$ desorbs a huge amount of CO_2 at 510°C (with trace CO) and 637°C (concomitantly with abundant CO; Fig. 3D), respectively assigned to the nondissociated CO_2 adsorption on the 3Ni-In sites and dissociated CO_2 adsorption on 3Ni-C sites on the $InNi_3C_{0.5}(111)$ plane (*23*). The $InNi_3C_{0.5}/SiO_2$ and $InNi_3C_{0.5}/a\text{-}ZrO_2$ catalysts also offer two CO_2 desorption peaks at 500°C (with trace CO) and 635°C (with comparable CO amount) (Fig. 3E), which are similar to the unsupported $InNi_3C_{0.5}$, indicating the weak EMSI between $InNi_3C_{0.5}$ and SiO_2 or *a*-ZrO_2. In contrast, the CO_2 desorption peak at 500°C becomes very weak for $InNi_3C_{0.5}/t\text{-}ZrO_2$ and vanishes for the $InNi_3C_{0.5}/m\text{-}ZrO_2$ catalysts, while the high-temperature CO_2/CO desorption at 650° to 660°C becomes stronger especially for $InNi_3C_{0.5}/m\text{-}ZrO_2$ with most CO formation from CO_2 dissociation (Fig. 3E). Notably, little CO_2 is desorbed below 500°C for these four catalysts, indicating the poor ability to adsorb CO_2 on supports even after loading $InNi_3C_{0.5}$. Therefore, CO_2 should be mainly adsorbed on the $InNi_3C_{0.5}$ surface for these four catalysts. In spite of almost identical total amount of CO_2 adsorption on $InNi_3C_{0.5}$, the CO desorption amount is very distinct: $InNi_3C_{0.5}/m\text{-}ZrO_2$ (111.5 μmol g^{-1}) > $InNi_3C_{0.5}/t\text{-}ZrO_2$ (50.7 μmol g^{-1}) > $InNi_3C_{0.5}/a\text{-}ZrO_2$ (39.8 μmol g^{-1}) > $InNi_3C_{0.5}/SiO_2$ (30.2 μmol g^{-1}) (table S6), consistent with the ZrO_2-type dependence of their EMSI strength. These results explicitly order the CO_2 dissociation activity of these four catalysts as follows: $InNi_3C_{0.5}/m\text{-}ZrO_2$ > $InNi_3C_{0.5}/t\text{-}ZrO_2$ > $InNi_3C_{0.5}/a\text{-}ZrO_2$ ~ $InNi_3C_{0.5}/SiO_2$. To further investigate the quantitative connection between the CO desorption amount and catalytic performance, the TOFs of these four catalysts are plotted against their CO desorption amount (Fig. 3F), showing a good linear correlation. On the basis of these results, we are confident that the discrepancy of the catalyst activity for the CO_2-to-methanol reaction is tightly linked with their different CO_2 dissociation activity that is governed by the ZrO_2 type–dependent EMSI between $InNi_3C_{0.5}$ and ZrO_2 supports.

In-depth understanding of ZrO_2 type–dependent EMSI: Density functional theory calculations

To further gain insight into the EMSI between $InNi_3C_{0.5}$ and ZrO_2 supports, first-principle calculations were performed. We first established two interfaces between $InNi_3C_{0.5}$ and perfect *m*-ZrO_2 or partially reduced *m*-ZrO_2 (denoted as *m*-ZrO_{2-x}) (Fig. 4A). Their electron density maps reveal that the electrons are accumulated to some extent at the $InNi_3C_{0.5}$–*m*-ZrO_2 interface but more accumulated at $InNi_3C_{0.5}$–*m*-ZrO_{2-x} along with the oxygen vacancy formation on *m*-ZrO_{2-x}, confirming the EMSI at the interface; electrons also redistribute similarly at $InNi_3C_{0.5}$–*t*-ZrO_2 and $InNi_3C_{0.5}$–*t*-ZrO_{2-x} interfaces (Fig. 4B), but with lower electron density than at the $InNi_3C_{0.5}$–*m*-ZrO_2 and $InNi_3C_{0.5}$–*m*-ZrO_{2-x} interfaces. These calculations indicate the strongest EMSI between $InNi_3C_{0.5}$ and *m*-ZrO_{2-x}, coinciding with the conclusions based on the XPS and DRIFTS results. Moreover, the electron structure of surface Ni is also affected, especially *d* electrons (see the evidences of projected density of states in Fig. 4C), making the CO_2 adsorption and concomitant dissociation ability of 3Ni-In close to that of 3Ni-C sites. The difference in the CO_2 adsorption energies on 3Ni-In and 3Ni-C is reduced from 0.47 eV on unsupported $InNi_3C_{0.5}(111)$ to 0.41, 0.39, 0.37, and 0.24 eV on $InNi_3C_{0.5}(111)$ surfaces supported on *m*-ZrO_2(−111), *t*-ZrO_2(011), *t*-ZrO_{2-x}(011), and *m*-ZrO_{2-x}(−111), respectively, again indicating the strongest EMSI between $InNi_3C_{0.5}(111)$ and *m*-ZrO_{2-x}(−111). Furthermore, the interfacial adhesion work (W_{ad}) of the four systems was also calculated, and $InNi_3C_{0.5}(111)/m\text{-}ZrO_{2-x}$(−111) exhibits the largest W_{ad} of 2.89 J/m^2, followed by $InNi_3C_{0.5}(111)/t\text{-}ZrO_{2-x}$(011), $InNi_3C_{0.5}(111)/m\text{-}ZrO_2$(−111), and $InNi_3C_{0.5}(111)/t\text{-}ZrO_2$(011), further consolidating the strongest EMSI between $InNi_3C_{0.5}(111)$ and *m*-ZrO_{2-x}(−111). This markedly enhanced EMSI between $InNi_3C_{0.5}$ and *m*-ZrO_2 imparts high CO_2 dissociation activity of the 3Ni-In sites quite comparable to the 3Ni-C sites, rationally explaining why $InNi_3C_{0.5}/m\text{-}ZrO_2$ offers a single strong CO_2/CO desorption peak in Fig. 3E. Also, the CO_2 chemical adsorption configurations are quite similar on the unsupported and ZrO_2-supported $InNi_3C_{0.5}$ surfaces (Fig. 4, D and E), and therefore, the difference in CO_2 adsorption energy on these systems is attributed to the electronic rather than geometrical effect.

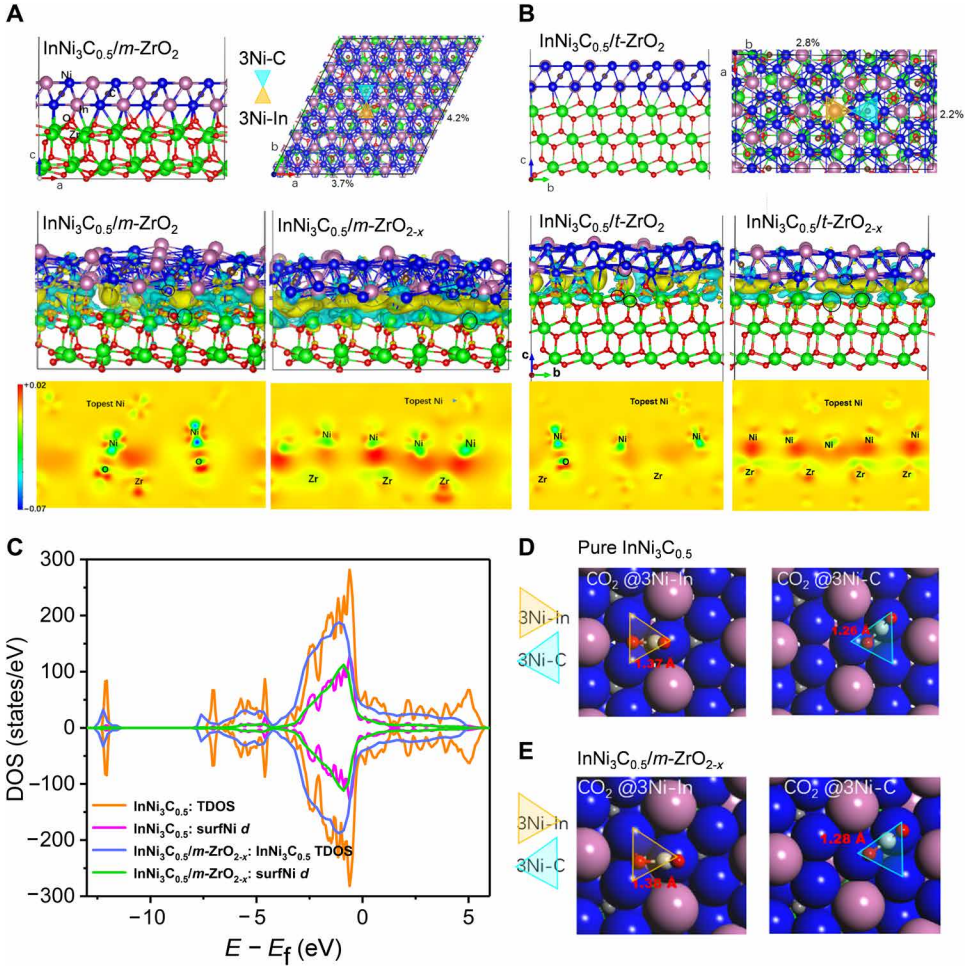

Fig. 4. Density functional theory studies. Three-dimensional (3D) interfacial configuration and electron density difference map for (**A**) $InNi_3C_{0.5}$/*m*-ZrO_2 (without oxygen deficiency) and $InNi_3C_{0.5}$/*m*-ZrO_{2-x}, and for (**B**) $InNi_3C_{0.5}$/*t*-ZrO_2 (without oxygen deficiency) and $InNi_3C_{0.5}$/*t*-ZrO_{2-x}. Top row: side view (left) and top view (right) of 3D interfacial unit cell. Middle row: depletion regions, blue; accumulation region, yellow. Bottom row: 2D configuration; cutting plane: the best plane of the chosen three atoms marked in circles in the middle 3D structures. (**C**) Total and partial density of states (TDOS and PDOS) for $InNi_3C_{0.5}$ and $InNi_3C_{0.5}$/*m*-ZrO_{2-x}. Chemically adsorbed CO_2 on 3Ni-In and 3Ni-C sites of (**D**) unsupported $InNi_3C_{0.5}$(111) surface and (**E**) defective *m*-ZrO_{2-x}(−111)–supported $InNi_3C_{0.5}$(111) surface. The C—O bond (the one parallel to the surface) length is provided.

Tailoring more advanced $InNi_3C_{0.5}$ catalyst

Inspired by above interesting findings, we believed that there is a possibility to build more advanced $InNi_3C_{0.5}$ catalysts via EMSI tailoring by using other oxides to replace *m*-ZrO_2. Given that the EMSI is tightly related to the reducible oxides enriched with oxygen vacancies, some universal transition metal oxides such as ZnO, TiO_2, CeO_2, and Fe_2O_3 were used to support $InNi_3C_{0.5}$ nanoparticles (Fig. 5A and fig. S11). In particular, $InNi_3C_{0.5}/Fe_3O_4$, obtained by carburization treatment of an In_2O_3-NiO/Fe_2O_3 precursor (details in Materials and Methods), delivers a superior performance over the other candidates, for example, enabling CO_2-to-methanol with 20.0% CO_2 conversion and 91.2% CH_3OH selectivity at 325°C, GHSV of 30,000 ml g_{cat}^{-1} $hour^{-1}$, H_2/CO_2 molar ratio of 8:1, and 4.0 MPa, and even with 25.7% CO_2 conversion and 90.2% CH_3OH selectivity at 325°C, GHSV of 36,000 ml g_{cat}^{-1} $hour^{-1}$, H_2/CO_2 molar ratio of 10:1, and 6.0 MPa (tables S4 and S7). Notably, no matter how harsh the reaction conditions became in the present work, methanol selectivity always stayed at 90 to 93% with CH_4 selectivity no more than 0.2%. The $InNi_3C_{0.5}/Fe_3O_4$ catalyst was further examined at 325°C and a fixed GHSV (for CO_2) of 10,500 ml g_{cat}^{-1} $hour^{-1}$ but varied reaction pressure and H_2/CO_2 molar ratio; excitingly, when increasing the reaction pressure and H_2/CO_2 molar ratio from 4.0 MPa and 3:1 up to 6.0 MPa and 10:1, the STY of methanol gradually increased from 1.35 (with 10.0% conversion and 90.0% selectivity) to 2.62 g_{MeOH} g_{cat}^{-1} $hour^{-1}$ (with 18.8% conversion and 92.8% selectivity; table S7). We also evaluated our $InNi_3C_{0.5}/Fe_3O_4$ catalyst under the reported reaction conditions, and obviously, the $InNi_3C_{0.5}/Fe_3O_4$ catalyst exhibited higher STY of methanol than the reported ones under the identical reaction conditions: for example, 1.01 versus 0.73 g_{MeOH} g_{cat}^{-1} $hour^{-1}$ for ZnO-ZrO_2 at 320°C, 5.0 MPa, H_2/CO_2 molar ratio of 3:1, and 24,000 ml g_{cat}^{-1} $hour^{-1}$ (*20*); 1.16 versus 0.86 g_{MeOH} g_{cat}^{-1} $hour^{-1}$ for In@Co at 300°C, 5.0 MPa, H_2/CO_2 molar ratio of 4:1, and 27,500 ml g_{cat}^{-1} $hour^{-1}$ (*39*); 1.30 versus 1.01 g_{MeOH} g_{cat}^{-1} $hour^{-1}$ for Pd-In_2O_3 at 280°C, 5.0 MPa, H_2/CO_2 molar ratio of 4:1, and 48,000 ml g_{cat}^{-1} $hour^{-1}$ (*40*); 0.308 versus 0.288 g_{MeOH} g_{cat}^{-1} $hour^{-1}$ for hexagonal In_2O_3 at 280°C, 5.0 MPa, H_2/CO_2 molar ratio of 6:1, and 9000 ml g_{cat}^{-1} $hour^{-1}$ (*41*). All things considered, such $InNi_3C_{0.5}/Fe_3O_4$ catalyst

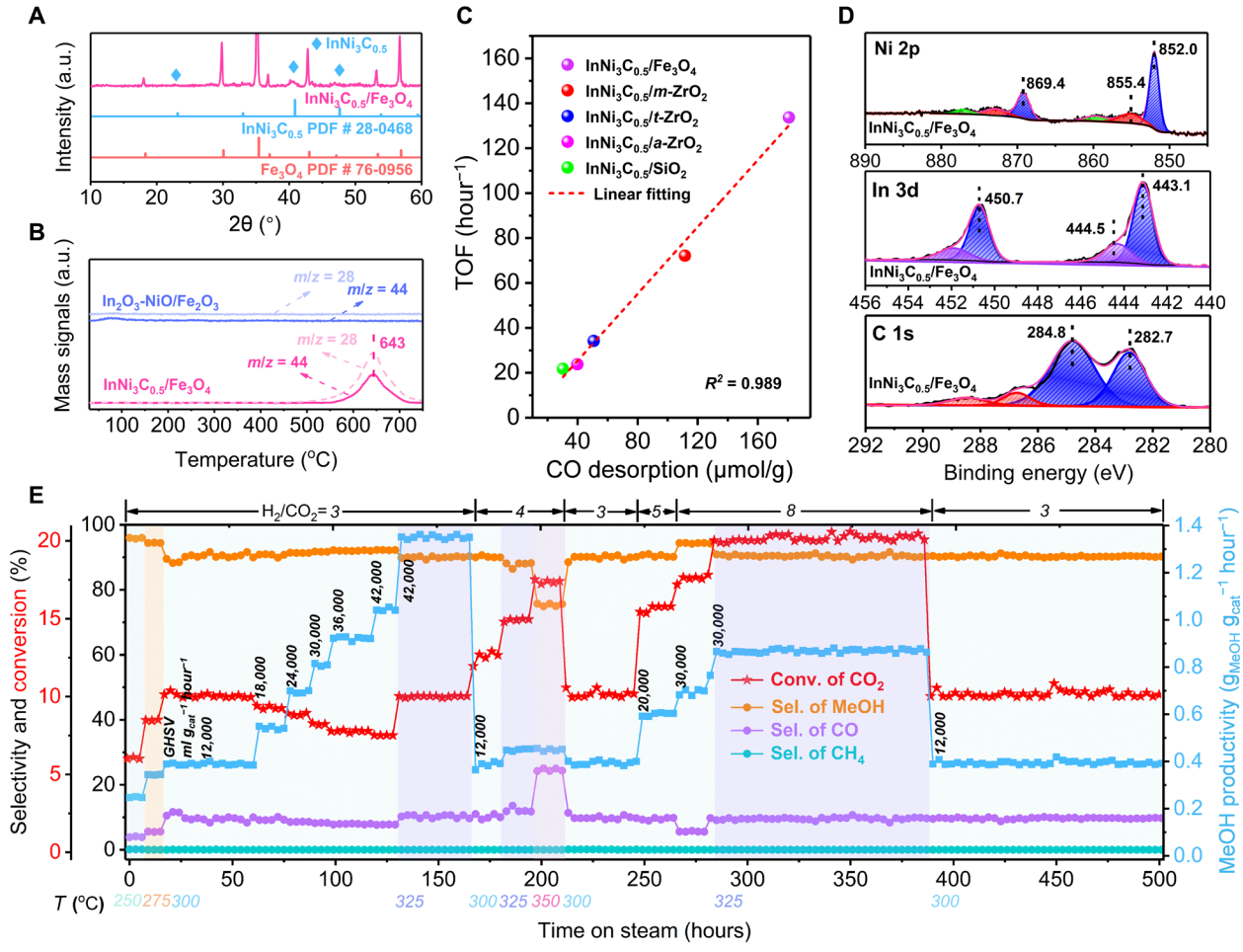

Fig. 5. Characterization and catalytic performance of $InNi_3C_{0.5}/Fe_3O_4$. (**A**) XRD patterns of the $InNi_3C_{0.5}/Fe_3O_4$ catalyst. (**B**) CO_2-TPD-MS profiles for In_2O_3-NiO/Fe_2O_3 catalyst precursor and $InNi_3C_{0.5}/Fe_3O_4$ catalyst. MS signal of the carbonaceous species for CO_2 desorption: CO_2 signal ($m/z = 44$) and CO signal ($m/z = 28$). (**C**) Plot of TOF as a function of the amount of CO desorption (reaction conditions for TOF calculations: 300°C, 4.0 MPa, $H_2/CO_2 = 3:1$, and GHSV = 24,000 ml g_{cat}^{-1} $hour^{-1}$). (**D**) XPS spectra in Ni 2p, In 3d, and C 1s regions of $InNi_3C_{0.5}/Fe_3O_4$. (**E**) CO_2 conversion and CH_3OH/CO/CH_4 selectivity along with the time on stream over the $InNi_3C_{0.5}/Fe_3O_4$ catalyst (temperature of 250° to 350°C, H_2/CO_2 of 3:1 to 8:1, and GHSV of 12,000 to 42,000 ml g_{cat}^{-1} $hour^{-1}$).

outperforms all ever-reported promising catalysts (*5*, *19*, *20*, *39*–*44*) in terms of methanol STY, methanol selectivity (>90%), and intrinsic activity represented by TOF [for example, 133.7 $hour^{-1}$ based on total number of active sites (3Ni-In and 3Ni-C) or 89.1 $hour^{-1}$ based on total number of surface Ni atoms for our $InNi_3C_{0.5}/Fe_3O_4$, higher than 74.2 $hour^{-1}$ based on total number of surface Cu atoms for Cu-Zn-ZrO_2 (*44*); see detailed comparison in table S4]. As expected, the $InNi_3C_{0.5}/Fe_3O_4$ catalyst exhibits further improved ability for CO_2 dissociative adsorption evidenced by much higher MS signal of CO than CO_2 in the CO_2-TPD profiles in comparison with the $InNi_3C_{0.5}/ZrO_2$ catalysts (Fig. 5, B and C, and table S6), thereby leading to a remarkable increase of the TOF to 133.7 $hour^{-1}$. This breakthrough is due to the strong EMSI between $InNi_3C_{0.5}$ and Fe_3O_4, evidenced by lowered binding energy values of In, Ni, and C in $InNi_3C_{0.5}$ (remarkably against unsupported $InNi_3C_{0.5}$ and slightly against $InNi_3C_{0.5}/m$-ZrO_2; Fig. 5D and table S5).

Moreover, $InNi_3C_{0.5}/Fe_3O_4$ offers a much smaller $InNi_3C_{0.5}$ particle size of 7 nm than that (~16 nm) of the $InNi_3C_{0.5}/ZrO_2$ catalysts. Coupling this feature with the markedly improved activity for $InNi_3C_{0.5}/Fe_3O_4$ leads to a big reduction of the loading of $InNi_3C_{0.5}$ to 11.4 weight % (wt %), almost one-fourth of that (42.8 wt %; table S8) of $InNi_3C_{0.5}/m$-ZrO_2. Low loading of In together with using cheap Fe_3O_4 as support makes $InNi_3C_{0.5}/Fe_3O_4$ more affordable, which is also an important consideration in practical application. Another advantage of our $InNi_3C_{0.5}$ nano-intermetallic catalysts is the promising stability (Fig. 5E and figs. S12 and S13), and especially the $InNi_3C_{0.5}/Fe_3O_4$ catalyst shows satisfying activity/selectivity maintenance throughout the entire 500-hour testing in a wide range of reaction conditions (Fig. 5E) without any sintering (fig. S12). Notably, no any FeC_x species was detected in the $InNi_3C_{0.5}/Fe_3O_4$ catalyst even after 500-hour testing, according to the ^{57}Fe Mössbauer spectroscopy and Fe 2p XPS spectra (fig. S14 and Supplementary Text). By comparison, most literature catalysts are suffering from rapid deactivation because of the easy carbon deposition and/or catalyst sintering (*15*, *45*, *46*), such as the conventional CuZnAl catalyst, which loses more than 50% of its initial activity within 100-hour reaction under the identical reaction conditions (*19*). Our $InNi_3C_{0.5}/Fe_3O_4$ catalyst also shows pleasing tolerance to sulfur poisoning even in the presence of 50 ppmv H_2S in the feed gas (fig. S15).

We demonstrate an outstanding oxide-supported $InNi_3C_{0.5}$ nanointermetallic catalyst for efficient methanol synthesis from CO_2. First, interesting ZrO_2 type–dependent activity of the $InNi_3C_{0.5}/ZrO_2$ catalysts is observed, which is tightly linked with the EMSI strength governed by the type of ZrO_2 phase. Evidenced by experimental CO_2-/H_2-TPD, XPS, EPR, CO-DRIFTS spectral studies, and density functional theory (DFT) calculations, $InNi_3C_{0.5}/m$-ZrO_2 achieves markedly enhanced EMSI that therefore endues $InNi_3C_{0.5}$ with high electron density, due to the higher oxygen deficiency of m-ZrO_2 compared to t-ZrO_2 and a-ZrO_2. As a result, the $InNi_3C_{0.5}/m$-ZrO_2 catalyst shows superior activity for dissociative adsorption of CO_2 and subsequent hydrogenation to form methanol over the two others. Inspired by this finding, a more advanced $InNi_3C_{0.5}/Fe_3O_4$ catalyst, with further enhanced EMSI effect, is developed via carburization of an In_2O_3-NiO/Fe_2O_3 precursor. As expected, over this catalyst, the CO_2 dissociative adsorption is markedly improved and therefore leads to a remarkable increase of the catalyst activity. This catalyst is also stable, highly resistant to sulfur poisoning, and cost-efficient because of the low In loading and cheap Fe_3O_4 support used. Our results will stimulate attempts to discover highly active/selective intermetallic catalysts by optimizing EMSI effect through combining theoretical and experimental studies, which might lead to commercial exploitation of an efficient CO_2 hydrogenation to methanol process.

MATERIALS AND METHODS

Catalyst preparation

Synthesis of zirconia supports

Three zirconia supports with different phases (monoclinic, tetragonal, and amorphous zirconia, denoted as m-ZrO_2, t-ZrO_2, and a-ZrO_2, respectively) were synthesized according to the following methods. m-ZrO_2 was synthesized by a precipitation method: $Zr(NO_3)_4{\cdot}5H_2O$ (6.968 g) was dissolved in deionized water (100 ml), followed by dropwise addition of a 100-ml aqueous solution of $(NH_4)_2CO_3$ (3.119 g) in 30 min under vigorous stirring at 70°C to form a precipitate. The suspension was continuously stirred at 70°C for 2 hours, followed by aging at ambient temperature overnight, filtering, and washing several times with deionized water. Subsequently, the as-obtained sample was dried at 110°C for 4 hours and calcined at 500°C in static air for 3 hours to yield the m-ZrO_2 support. The t-ZrO_2 was synthesized by a combined precipitation and reflux digestion method (*47*): $ZrOCl_2{\cdot}8H_2O$ (16.106 g) was dissolved in deionized water (100 ml), followed by dropwise adding 200-ml NH_4OH solution (1 M) under vigorous stirring. The resulting material was heated in the mother liquor at 105°C under reflux for 240 hours, while the pH was maintained at 10, followed by aging, filtering, washing (until to no detectable chlorine anions in the filtrate by $AgNO_3$), drying at 110°C for 4 hours, and calcining at 800°C in static air for 3 hours to yield the t-ZrO_2 support. a-ZrO_2 was synthesized by a precipitation method assisted with surfactant (*30*, *48*): Pluronic P123 ($EO_{20}PO_{70}EO_{20}$, 6.960 g) and $ZrOCl_2{\cdot}8H_2O$ (13.075 g) were dissolved in deionized water (200 ml) with vigorous stirring at 80°C; subsequently, a NH_4OH solution (1 M) was dropwise added to the obtained solution until a pH of 11. The obtained suspension was digested at 100°C for 240 hours, followed by aging at ambient temperature overnight, filtering, washing several times with deionized water, and drying at 110°C for 12 hours. Last, the product was calcined for 4 hours at 450°C in static air to obtain the a-ZrO_2 support.

Synthesis of supported InNi3C0.5 catalysts

The $InNi_3C_{0.5}/m$-ZrO_2 catalyst was taken as an example to describe the synthesis procedures (fig. S16): First, $In(NO_3)_3{\cdot}4H_2O$ (0.487 g) and $Ni(NO_3)_2{\cdot}6H_2O$ (1.140 g) were dissolved in deionized water (1.500 g) under stirring at ambient temperature for 15 min. Then, the as-prepared m-ZrO_2 support (0.500 g) was impregnated with the as-obtained aqueous solution, followed by ultrasonication for 2 hours, aging at ambient temperature overnight, drying in air at 100°C for 12 hours, and calcining in static air at 350°C for 2 hours. Then, the resulting In_2O_3-NiO-ZrO_2 catalyst precursor was packed into a continuous-flow fixed-bed tubular reactor made of stainless steel (inner diameter of 8 mm with length of 768 mm) and carburized in a stream of a mixture of H_2 and CO_2 (30 ml min^{-1}, H_2/CO_2 molar ratio of 3:1) at 600°C for 3 hours under atmospheric pressure. $InNi_3C_{0.5}/t$-ZrO_2, $InNi_3C_{0.5}/a$-ZrO_2, $InNi_3C_{0.5}/SiO_2$ (for comparison; commercial SiO_2, Sinopharm Chemical Reagent Co. Ltd.), and $InNi_3C_{0.5}/MO_x$ (MO_x = ZnO, TiO_2, CeO_2, and Fe_3O_4) were synthesized following the same procedures. The catalysts with different $InNi_3C_{0.5}$ loadings were obtained by varying the adding amounts of indium nitrate and nickel nitrate precursors (table S8).

Catalyst characterization

X-ray powder diffraction (XRD) measurements were conducted on a Rigaku Ultima IV diffractometer (Japan), using a Cu Kα radiation source generated at 30 kV and 25 mA in the 2θ angle range of 10° to 60° at a scanning speed of 10° min^{-1} with a step size of 0.02°. The catalyst micromorphology and nanostructure were observed by a scanning electron microscope (Hitachi S-4800, Japan; accelerating voltage: 3.0 kV) and TEM (FEI-Tecnai G2 F30, USA; accelerating voltage: 200 kV). Nitrogen adsorption-desorption isotherms were taken on a Quantachrome Autosorb-3B instrument (USA) at −196°C. The samples were evacuated at 300°C for at least 6 hours before the measurements. The SSA was calculated from the adsorption branch using standard Brunauer-Emmett-Teller theory. The pore size distribution and total pore volume were determined using the Barrett-Joyner-Halenda method based on the adsorption isotherm. Quasi–in situ XPS analyses were carried out on an AXIS SUPRA system (Shimadzu/Kratos) equipped with an in situ reactor chamber, using a standard Al Kα x-ray source (300 W) with an analyzer pass energy of 40.0 eV. The circular catalyst chips (1.5 mm diameter) were pretreated in H_2/CO_2 mixture (H_2/CO_2 molar ratio of 3:1, 30 ml min^{-1}) at 300°C for 2 hours in the reactor chamber and then cooled down to room temperature and transferred into the spectrometer chamber without exposure into air. All binding energies were referenced to the adventitious C1s line at 284.8 eV. EPR was performed on a Bruker EMXPLUS spectrometer at a microwave frequency of 9.83 GHz (X-band) with catalyst sample of 0.038 g. Spectra were collected accumulating 1 scan for field sweeps of 5000 G at −196°C with a microwave power of 0.2 mW. The ^{57}Fe Mössbauer spectra were recorded on a conventional spectrometer (Wissel MS-500, Germany) in transmission geometry with constant acceleration mode. ^{57}Co(Pd) was used as the radioactive source. The spectra were fitted with the appropriate superposition of Lorentzian lines. The real In and Ni contents of the $InNi_3C_{0.5}$ catalysts were quantitatively analyzed by the inductively coupled plasma–atomic emission spectroscopy on Optima 8300 (PerkinElmer, USA).

H_2 and CO_2 TPD (H_2-/CO_2-TPD) measurements were performed on a TP 5080 multifunctional automatic adsorption/desorption instrument (Xianquan Industrial and Trading Co. Ltd., P.R. China)

with a TCD and an online mass spectrometer (ProLine Dycor, AMETEK Process Instrument, USA). For each trial, the sample (0.1 g) was treated in a H_2 flow (30 ml min^{-1}) at 300°C for 1 hour and flushed by a He flow (30 ml min^{-1}) at 300°C for 30 min to clean its surface. After cooling to room temperature in a He flow, the catalyst sample was exposed to a H_2 (or CO_2) flow for 30 min for saturation adsorption of H_2 (or CO_2), and afterward, the carrier gas (ultrahighly purified N_2 for H_2-TPD or He for CO_2-TPD) was switched into the reactor at a flow rate of 30 ml min^{-1} until stable baseline appeared before implementing. The TPD profiles were then recorded from room temperature to 850°C at a heating rate of 10°C min^{-1}.

In situ DRIFTS experiments for CO adsorption on the catalysts were carried out on a Bruker Tensor 27 spectrometer, equipped with a mercury-cadmium-telluride detector and a Harrick Scientific HV-CDRP-4 reaction cell fitted with ZnSe windows. The catalyst sample of 0.020 g was placed into the cell chamber, treated at 400°C for 2 hours in a H_2 flow (30 ml min^{-1}), purged with a He flow (30 ml min^{-1}) at 400°C for 1 hour, and cooled down to room temperature in He for taking a reference spectrum. Then, the catalyst was exposed to pure CO flow (10 ml min^{-1}) for 30 min and subsequently purged with He (30 ml min^{-1}) for 30 min, for taking CO-DRIFT spectrum. All spectra were recorded by collecting 32 scans from 4000 to 400 cm^{-1} at a resolution of 4 cm^{-1}.

Reactivity tests

The CO_2-to-methanol reaction was evaluated in a continuous-flow fixed-bed tubular reactor made of stainless steel (inner diameter of 8 mm with length of 768 mm) that was heated by an electronic furnace. Typically, the as-carburized catalyst with granule size between 100 and 125 μm (0.500 ± 0.002 g) was packed into the reactor, and the catalyst bed at the center of the reactor was supported by quartz wool at both ends. The reaction temperature, pressure, GHSV, and H_2/CO_2 molar ratio were varied in the range of 250° to 350°C, 1.0 to 6.0 MPa, 12,000 to 115,500 ml g_{cat}^{-1} $hour^{-1}$, and 3:1 to 10:1, respectively.

The effluent gas was quantitatively analyzed by an online Agilent 7820 gas chromatograph equipped with a thermal conductivity detector (TCD) and a flame ionization detector. The postreactor line was maintained at 150°C to prevent product from condensing. All the reaction data were collected after running for at least 3 hours under steady-state conditions. The gas sample was withdrawn every 30 min, and more than eight measurements were taken for each reaction parameter. The products from this reaction were CH_3OH, CO, and CH_4. The CO_2 conversion (%) and product selectivity (%) were calculated by the standard normalization method based on carbon atom balance according to the following equations

$$CO_2\ \text{conversion}\ (\%) = \left(1 - \frac{f_{CO_2} A_{CO_2,out}}{\sum f_i A_{i,out} + f_{CO_2} A_{CO_2,out}}\right) \times 100\%$$

$$\text{i selectivity}\ (\%) = \left(\frac{f_i A_{i,out}}{\sum f_i A_{i,out}}\right) \times 100\%$$

where $A_{i,out}$ and f_i are the chromatographic peak area at the outlet and the relative molar calibration factor of the individual product i (i: CH_3OH, CO, and CH_4), respectively.

STY of methanol, expressed as grams of CH_3OH per gram catalyst per hour (g_{MeOH} g_{cat}^{-1} $hour^{-1}$), was calculated according to the following equation

$$CH_3OH\ STY = \frac{F_{CO_2,in} \times X_{CO_2} \times S_{CH_3OH} \times MW_{CH_3OH}}{W_{cat} \times V_m}$$

where $F_{CO2,in}$ is the volumetric flow rate of CO_2 (milliliter $hour^{-1}$), X_{CO2} is the CO_2 conversion, S_{CH3OH} is the CH_3OH selectivity, MW_{CH3OH} is the molecular weight of CH_3OH (32 g mol^{-1}), W_{cat} is the overall mass of catalyst (g), and V_m is the ideal molar volume of CO_2 at standard temperature and pressure.

Thermodynamic analysis and TOF calculations

The thermodynamic analysis was performed by using the HSC Chemistry 6.0 software, with the results shown in fig. S6. In the analysis, the reaction pressure was increased from 0 to 100 bar (10 MPa) at different temperatures (from 200° to 400°C). The reactants of H_2 and CO_2 (with the molar ratio of 3:1) and aimed products CH_3OH and H_2O were considered ($CO_{2(g)} + 3H_{2(g)} \leftrightarrow CH_3OH_{(g)} + H_2O_{(g)}$). The theoretical equilibrium conversion of CO_2 (X_e) was calculated according to the following equation

$$X_e = \left(\frac{A - A_0}{A}\right) \times 100\%$$

where A is the initial amount of CO_2 (kmol) and A_0 is the amount of CO_2 (kmol) at thermodynamic equilibrium.

To assess the intrinsic activity of the supported $InNi_3C_{0.5}$ catalysts for the CO_2-to-methanol reaction, the TOF was measured (with CO_2 conversion below 10.0% at 300°C, 4.0 MPa, and 24,000 ml g_{cat}^{-1} $hour^{-1}$; table S3), which was defined as the produced methanol per active site per hour

$$TOF = \frac{\frac{F_{CO_2}}{V_m} \times X_{CO_2} \times S_{CH_3OH} \times N_A}{W_{cat} \times x \times N_{mum}}$$

where F_{CO2} is the volumetric flow rate of CO_2 (milliliter $hour^{-1}$), V_m is the ideal molar volume of CO_2 at standard temperature and pressure, X_{CO2} is the CO_2 conversion, S_{CH3OH} is the CH_3OH selectivity, N_A is the Avogadro constant, W_{cat} is the mass (0.5 g) of the supported $InNi_3C_{0.5}$ catalysts, and x is the mass fraction (42.8%) of $InNi_3C_{0.5}$ in the supported $InNi_3C_{0.5}$ catalysts. N_{num} is the number of available surface active sites (i.e., the total number of 3Ni-In and 3Ni-C) per gram $InNi_3C_{0.5}$, which can be calculated according to the following equation (*23*)

$$N_{num} = \frac{SA \times 25.0\%}{A_{(3Ni\text{-}In\ or\ 3Ni\text{-}C)}}$$

where SA is the exposed SSA (m^2 g^{-1}) of the $InNi_3C_{0.5}$ nanoparticles in the supported $InNi_3C_{0.5}$ catalyst [assuming that all exposed surfaces of the supported $InNi_3C_{0.5}$ nanoparticles were $InNi_3C_{0.5}$ (111) surface], 25.0% is the percentage of the total area of the surface active sites (the 3Ni-In and 3Ni-C sites) in the total surface area of $InNi_3C_{0.5}$ (111) surface, and $A_{(3Ni\text{-}In\ or\ 3Ni\text{-}C)}$ is the area of one 3Ni-In or 3Ni-C active site (one 3Ni-In site has equal area to one 3Ni-C site

of 3.013×10^{-20} m^2). The SA can be estimated on the basis of their TEM-visualized particle size according to the following equation (*3*)

$$SA = \frac{6}{\rho \times d_{InNi_3C_{0.5}}}$$

where ρ is the density of bulk $InNi_3C_{0.5}$. The corresponding TEM-visualized particle size distribution of $InNi_3C_{0.5}$ nanoparticles is shown in Fig. 1 (B to D) and table S1.

DFT calculations

We used spin-polarized DFT as implemented in the Vienna Ab initio Package. The self-interaction problem inherent with this functional has been partly removed by applying the DFT + U approach, where the Hubbard's U parameter for the 4d orbitals of the Zr ions was set to 4 eV (*49*). Core-valence and electron-electron interactions were treated by the projector augmented wave method (*50*) and the Perdew-Burke-Ernzerhof generalized gradient approximation (*51*, *52*). The energy cutoff for the planewave basis set was 400 eV. Geometry optimization was considered to be converged when the forces was <0.03 eV/Å. Reciprocal space was sampled only at the Γ-point because of the large supercell. The interface structure of $InNi_3C_{0.5}(111)/t\text{-}ZrO_2(011)$ was constructed using (2 × 4) $InNi_3C_{0.5}(111)$ and (3 × 3) $t\text{-}ZrO_2(011)$ with the lattice mismatch less than 3%, and the interface structure of $InNi_3C_{0.5}(111)/m\text{-}ZrO_2(-111)$ was constructed using (4 × 4) $InNi_3C_{0.5}(111)$ and (3 × 3) $m\text{-}ZrO_2(-111)$ with the lattice mismatch ~4% (Fig. 4, A and B). The bottom Ni at the left corner of $InNi_3C_{0.5}(111)$ was used as the reference atom to construct different interfacial structures at top site of O, top site of Zr, and bridge site of O-Zr of ZrO_2. Three-layer thickness of $InNi_3C_{0.5}$ was chosen to build the interfacial structures to save the cost of the computation where the interfacial structures of $InNi_3C_{0.5}(111)/m\text{-}ZrO_2(-111)$ contain 360 atoms and the geometry optimization is very time-consuming and presents an experimental weight ratio of about 1:1 with the ZrO_2 support. All atoms of $InNi_3C_{0.5}$ and the top ZrO_2 unit were allowed to relax. For the defective interfacial structures, the interfacial oxygen atoms were removed yielding an oxygen vacancy of 31.25 and 22%, close to the experimental value of ~30 and ~24% for $InNi_3C_{0.5}/m\text{-}ZrO_{2-x}$ and $InNi_3C_{0.5}/t\text{-}ZrO_{2-x}$, respectively (the oxygen vacancy concentration was calculated according to XPS results; see table S5, fig. S9, and Supplementary Text).

To describe the interfacial binding strength qualitatively, the ideal adhesion work of the interface was defined as follows (*53*)

$$W_{ad} = \frac{E_{ZrO_2} + E_{InNi_3C_{0.5}} - E_{InNi_3C_{0.5}/ZrO_2}}{A}$$

The first, second, and third terms on the right side of the equation are the total energies of the optimized single ZrO_2 surface, single $InNi_3C_{0.5}$, and $InNi_3C_{0.5}/ZrO_2$ interface, respectively. *A* is the interfacial area. The larger the adhesion work, the stronger the interfacial binding of $InNi_3C_{0.5}$ with ZrO_2.

SUPPLEMENTARY MATERIALS

Supplementary material for this article is available at http://advances.sciencemag.org/cgi/content/full/7/32/eabi6012/DC1

REFERENCES AND NOTES

1. P. Falkowski, R. J. Scholes, E. Boyle, J. Canadell, D. Canfield, J. Elser, N. Gruber, K. Hibbard, P. Högberg, S. Linder, F. T. Mackenzie, B. Moore III, T. Pedersen, Y. Rosenthal, S. Seitzinger, V. Smetacek, W. Steffen, The global carbon cycle: A test of our knowledge of earth as a system. *Science* **290**, 291–296 (2000).
2. B. M. Tackett, E. Gomez, J. G. Chen, Net reduction of CO_2 via its thermocatalytic and electrocatalytic transformation reactions in standard and hybrid processes. *Nat. Catal.* **2**, 381–386 (2019).
3. P. Gao, S. Li, X. Bu, S. Dang, Z. Liu, H. Wang, L. Zhong, M. Qiu, C. Yang, J. Cai, W. Wei, Y. Sun, Direct conversion of CO_2 into liquid fuels with high selectivity over a bifunctional catalyst. *Nat. Chem.* **9**, 1019–1024 (2017).
4. F. P. García de Arquer, C.-T. Dinh, A. Ozden, J. Wicks, C. McCallum, A. R. Kirmani, D.-H. Nam, C. Gabardo, A. Seifitokaldani, X. Wang, Y. C. Li, F. Li, J. Edwards, L. J. Richter, S. J. Thorpe, D. Sinton, E. H. Sargent, CO_2 electrolysis to multicarbon products at activities greater than 1 A cm^{-2}. *Science* **367**, 661–666 (2020).
5. J. Graciani, K. Mudiyanselage, F. Xu, A. E. Baber, J. Evans, S. D. Senanayake, D. J. Stacchiola, P. Liu, J. Hrbek, J. Fernandez Sanz, J. A. Rodriguez, Highly active copper-ceria and copper-ceria-titania catalysts for methanol synthesis from CO_2. *Science* **345**, 546–550 (2014).
6. G. A. Olah, Beyond oil and gas: The methanol economy. *Angew. Chem. Int. Ed.* **44**, 2636–2639 (2005).
7. M. Behrens, F. Studt, I. Kasatkin, S. Kühl, M. Hävecker, F. Abild-Pedersen, S. Zander, F. Girgsdies, P. Kurr, B.-L. Kniep, M. Tovar, R. W. Fischer, J. K. Nørskov, R. Schlögl, The active site of methanol synthesis over $Cu/ZnO/Al_2O_3$ industrial catalysts. *Science* **336**, 893–897 (2012).
8. A. González-Garay, M. S. Frei, A. Al-Qahtani, C. Mondelli, G. Guillén-Gosálbez, J. Pérez-Ramírez, Plant-to-planet analysis of CO_2-based methanol processes. *Energ. Environ. Sci.* **12**, 3425–3436 (2019).
9. B. C. H. Steele, A. Heinzel, Materials for fuel-cell technologies. *Nature* **414**, 345–352 (2001).
10. X. Jiang, X. Nie, X. Guo, C. Song, J. G. Chen, Recent advances in carbon dioxide hydrogenation to methanol via heterogeneous catalysis. *Chem. Rev.* **120**, 7984–8034 (2020).
11. L. Wang, M. Ghoussoub, H. Wang, Y. Shao, W. Sun, A. A. Tountas, T. E. Wood, H. Li, J. Y. Y. Loh, Y. Dong, M. Xia, Y. Li, S. Wang, J. Jia, C. Qiu, C. Qian, N. P. Kherani, L. He, X. Zhang, G. A. Ozin, Photocatalytic hydrogenation of carbon dioxide with high selectivity to methanol at atmospheric pressure. *Joule* **2**, 1369–1381 (2018).
12. J. Kothandaraman, A. Goeppert, M. Czaun, G. A. Olah, G. K. S. Prakash, Conversion of CO_2 from air into methanol using a polyamine and a homogeneous ruthenium catalyst. *J. Am. Chem. Soc.* **138**, 778–781 (2016).
13. S. Kattel, P. J. Ramírez, J. G. Chen, J. A. Rodriguez, P. Liu, Active sites for CO_2 hydrogenation to methanol on Cu/ZnO catalysts. *Science* **355**, 1296–1299 (2017).
14. S. Kattel, B. Yan, Y. Yang, J. G. Chen, P. Liu, Optimizing binding energies of key intermediates for CO_2 hydrogenation to methanol over oxide-supported copper. *J. Am. Chem. Soc.* **138**, 12440–12450 (2016).
15. J. Wu, M. Saito, M. Takeuchi, T. Watanabe, The stability of Cu/ZnO-based catalysts in methanol synthesis from a CO_2-rich feed and from a CO-rich feed. *Appl. Catal. A Gen.* **218**, 235–240 (2001).
16. N. Rui, Z. Wang, K. Sun, J. Ye, Q. Ge, C.-J. Liu, CO_2 hydrogenation to methanol over Pd/In_2O_3: Effects of Pd and oxygen vacancy. *Appl. Catal. B* **218**, 488–497 (2017).
17. Y. Hartadi, D. Widmann, R. J. Behm, Methanol synthesis via CO_2 hydrogenation over a Au/ZnO catalyst: An isotope labelling study on the role of CO in the reaction process. *Phys. Chem. Chem. Phys.* **18**, 10781–10791 (2016).
18. X. Yang, S. Kattel, S. D. Senanayake, J. A. Boscoboinik, X. Nie, J. Graciani, J. A. Rodriguez, P. Liu, D. J. Stacchiola, J. G. Chen, Low pressure CO_2 hydrogenation to methanol over gold nanoparticles activated on a CeO_x/TiO_2 interface. *J. Am. Chem. Soc.* **137**, 10104–10107 (2015).
19. M. Oliver, A. J. Martín, C. Mondelli, S. Mitchell, T. F. Segawa, R. Hauert, C. Drouilly, D. Curulla-Ferré, J. Pérez-Ramírez, Indium oxide as a superior catalyst for methanol synthesis by CO_2 hydrogenation. *Angew. Chem. Int. Ed.* **55**, 6261–6265 (2016).
20. J. Wang, G. Li, Z. Li, C. Tang, Z. Feng, H. An, H. Liu, T. Liu, C. Li, A highly selective and stable ZnO-ZrO_2 solid solution catalyst for CO_2 hydrogenation to methanol. *Sci. Adv.* **3**, e1701290 (2017).
21. F. Studt, I. Sharafutdinov, F. Abild-Pedersen, C. F. Elkjær, J. S. Hummelshøj, S. Dahl, I. Chorkendorff, J. K. Nørskov, Discovery of a Ni-Ga catalyst for carbon dioxide reduction to methanol. *Nat. Chem.* **6**, 320–324 (2014).
22. A. García-Trenco, A. Regoutz, E. R. White, D. J. Payne, M. S. P. Shaffer, C. K. Williams, PdIn intermetallic nanoparticles for the hydrogenation of CO_2 to methanol. *Appl. Catal. B* **220**, 9–18 (2018).
23. P. Chen, G. Zhao, X.-R. Shi, J. Zhu, J. Ding, Y. Lu, Nano-intermetallic $InNi_3C_{0.5}$ compound discovered as a superior catalyst for CO_2 reutilization. *iScience* **17**, 315–324 (2019).
24. C. T. Campbell, Electronic perturbations. *Nat. Chem.* **4**, 597–598 (2012).
25. A. Bruix, J. A. Rodriguez, P. J. Ramírez, S. D. Senanayake, J. Evans, J. B. Park, D. Stacchiola, P. Liu, J. Hrbek, F. Illas, A new type of strong metal–support interaction and the production of H_2 through the transformation of water on $Pt/CeO_2(111)$ and $Pt/CeO_x/TiO_2(110)$ catalysts. *J. Am. Chem. Soc.* **134**, 8968–8974 (2012).

26. S. Li, Y. Xu, Y. Chen, W. Li, L. Lin, M. Li, Y. Deng, X. Wang, B. Ge, C. Yang, S. Yao, J. Xie, Y. Li, X. Liu, D. Ma, Tuning the selectivity of catalytic carbon dioxide hydrogenation over iridium/cerium oxide catalysts with a strong metal–support interaction. *Angew. Chem. Int. Ed.* **56**, 10761–10765 (2017).
27. J. A. Rodriguez, P. Liu, D. J. Stacchiola, S. D. Senanayake, M. G. White, J. G. Chen, Hydrogenation of CO_2 to methanol: Importance of metal–oxide and metal–carbide interfaces in the activation of CO_2. *ACS Catal.* **5**, 6696–6706 (2015).
28. M. V. Ganduglia-Pirovano, A. Hofmann, J. Sauer, Oxygen vacancies in transition metal and rare earth oxides: Current state of understanding and remaining challenges. *Surf. Sci. Rep.* **62**, 219–270 (2007).
29. J. Ni, W. Leng, J. Mao, J. Wang, J. Lin, D. Jiang, X. Li, Tuning electron density of metal nickel by support defects in Ni/ZrO_2 for selective hydrogenation of fatty acids to alkanes and alcohols. *Appl. Catal. B* **253**, 170–178 (2019).
30. M. Rezaei, S. M. Alavi, S. Sahebdelfar, P. Bai, X. Liu, Z.-F. Yan, CO_2 reforming of CH_4 over nanocrystalline zirconia-supported nickel catalysts. *Appl. Catal. B* **77**, 346–354 (2008).
31. A. W. C. Lin, N. R. Armstrong, T. Kuwana, X-ray photoelectron/Auger electron spectroscopic studies of tin and indium metal foils and oxides. *Anal. Chem.* **49**, 1228–1235 (1977).
32. S. Dang, P. Gao, Z. Liu, X. Chen, C. Yang, H. Wang, L. Zhong, S. Li, Y. Sun, Role of zirconium in direct CO_2 hydrogenation to lower olefins on oxide/zeolite bifunctional catalysts. *J. Catal.* **364**, 382–393 (2018).
33. S. A. Steiner III, T. F. Baumann, B. C. Bayer, R. Blume, M. A. Worsley, W. J. MoberlyChan, E. L. Shaw, R. Schlögl, A. J. Hart, S. Hofmann, B. L. Wardle, Nanoscale zirconia as a nonmetallic catalyst for graphitization of carbon and growth of single- and multiwall carbon nanotubes. *J. Am. Chem. Soc.* **131**, 12144–12154 (2009).
34. X. Ke, G. J. Kramer, O. M. Løvvik, The influence of electronic structure on hydrogen absorption in palladium alloys. *J. Phys. Condens. Matter* **16**, 6267–6277 (2004).
35. A. G. Sato, D. P. Volanti, D. M. Meira, S. Damyanova, E. Longo, J. M. C. Bueno, Effect of the ZrO_2 phase on the structure and behavior of supported Cu catalysts for ethanol conversion. *J. Catal.* **307**, 1–17 (2013).
36. H.-Y. T. Chen, S. Tosoni, G. Pacchioni, Hydrogen adsorption, dissociation, and spillover on Ru_{10} clusters supported on anatase TiO_2 and tetragonal ZrO_2 (101) surfaces. *ACS Catal.* **5**, 5486–5495 (2015).
37. C. Yang, C. Pei, R. Luo, S. Liu, Y. Wang, Z. Wang, Z.-J. Zhao, J. Gong, Strong electronic oxide–support interaction over In_2O_3/ZrO_2 for highly selective CO_2 hydrogenation to methanol. *J. Am. Chem. Soc.* **142**, 19523–19531 (2020).
38. J. Zhang, H. Wang, L. Wang, S. Ali, C. Wang, L. Wang, X. Meng, B. Li, D. S. Su, F.-S. Xiao, Wet-chemistry strong metal–support interactions in titania-supported Au catalysts. *J. Am. Chem. Soc.* **141**, 2975–2983 (2019).
39. A. Bavykina, I. Yarulina, A. J. Al Abdulghani, L. Gevers, M. N. Hedhili, X. Miao, A. R. Galilea, A. Pustovarenko, A. Dikhtiarenko, A. Cadiau, A. Aguilar-Tapia, J.-L. Hazemann, S. M. Kozlov, S. Oud-Chikh, L. Cavallo, J. Gascon, Turning a methanation Co catalyst into an In–Co methanol producer. *ACS Catal.* **9**, 6910–6918 (2019).
40. M. S. Frei, C. Mondelli, R. García-Muelas, K. S. Kley, B. Puértolas, N. López, O. V. Safonova, J. A. Stewart, D. Curulla Ferré, J. Pérez-Ramírez, Atomic-scale engineering of indium oxide promotion by palladium for methanol production via CO_2 hydrogenation. *Nat. Commun.* **10**, 3377 (2019).
41. S. Dang, B. Qin, Y. Yang, H. Wang, J. Cai, Y. Han, S. Li, P. Gao, Y. Sun, Rationally designed indium oxide catalysts for CO_2 hydrogenation to methanol with high activity and selectivity. *Sci. Adv.* **6**, eaaz2060 (2020).
42. L. Wang, E. Guan, Y. Wang, L. Wang, Z. Gong, Y. Cui, X. Meng, B. C. Gates, F.-S. Xiao, Silica accelerates the selective hydrogenation of CO_2 to methanol on cobalt catalysts. *Nat. Commun.* **11**, 1033 (2020).
43. K. Chang, T. Wang, J. G. Chen, Hydrogenation of CO_2 to methanol over $CuCeTiO_x$ catalysts. *Appl. Catal. B* **206**, 704–711 (2017).
44. Y. Wang, S. Kattel, W. Gao, K. Li, P. Liu, J. G. Chen, H. Wang, Exploring the ternary interactions in Cu–ZnO–ZrO_2 catalysts for efficient CO_2 hydrogenation to methanol. *Nat. Commun.* **10**, 1166 (2019).
45. J. T. Sun, I. S. Metcalfe, M. Sahibzada, Deactivation of Cu/ZnO/Al_2O_3 methanol synthesis catalyst by sintering. *Ind. Eng. Chem. Res.* **38**, 3868–3872 (1999).
46. G. Prieto, J. Zečević, H. Friedrich, K. P. de Jong, P. E. de Jongh, Towards stable catalysts by controlling collective properties of supported metal nanoparticles. *Nat. Mater.* **12**, 34–39 (2013).
47. M. D. Rhodes, A. T. Bell, The effects of zirconia morphology on methanol synthesis from CO and H_2 over Cu/ZrO_2 catalysts: Part I. Steady-state studies. *J. Catal.* **233**, 198–209 (2005).
48. X. Zhang, M. Zhang, J. Zhang, Q. Zhang, N. Tsubaki, Y. Tan, Y. Han, Methane decomposition and carbon deposition over Ni/ZrO_2 catalysts: Comparison of amorphous, tetragonal, and monoclinic zirconia phase. *Int. J. Hydrogen Energy* **44**, 17887–17899 (2019).
49. H. V. Thang, G. Pacchioni, On the real nature of Rh single-atom catalysts dispersed on the ZrO_2 surface. *ChemCatChem* **12**, 2595–2604 (2020).
50. G. Kresse, D. Joubert, From ultrasoft pseudopotentials to the projector augmented-wave method. *Phys. Rev. B* **59**, 1758–1775 (1999).
51. J. P. Perdew, K. Burke, M. Ernzerhof, Generalized gradient approximation made simple. *Phys. Rev. Lett.* **77**, 3865–3868 (1996).
52. S. N. Steinmann, C. Corminboeuf, A generalized-gradient approximation exchange hole model for dispersion coefficients. *J. Chem. Phys.* **134**, 044117 (2011).
53. X.-R. Shi, S. Huang, Y. Huang, Y. Zhang, S. Zong, S. Xu, Y. Chen, P. Ma, Atomic structures and electronic properties of Ni or N modified Cu/diamond interface. *J. Phys. Condens. Matter* **32**, 225001 (2020).
54. A. Machocki, T. Ioannides, B. Stasinska, W. Gac, G. Avgouropoulos, D. Delimaris, W. Grzegorczyk, S. Pasieczna, Manganese–lanthanum oxides modified with silver for the catalytic combustion of methane. *J. Catal.* **227**, 282–296 (2004).
55. S. Ponce, M. A. Peña, J. L. G. Fierro, Surface properties and catalytic performance in methane combustion of Sr-substituted lanthanum manganites. *Appl Catal B* **24**, 193–205 (2000).
56. M. Zhang, J. Zhang, Y. Wu, J. Pan, Q. Zhang, Y. Tan, Y. Han, Insight into the effects of the oxygen species over Ni/ZrO_2 catalyst surface on methane reforming with carbon dioxide. *Appl. Catal. B* **244**, 427–437 (2019).
57. N. Rui, F. Zhang, K. Sun, Z. Liu, W. Xu, E. Stavitski, S. D. Senanayake, J. A. Rodriguez, C.-J. Liu, Hydrogenation of CO_2 to methanol on a $Au^{\delta+}$–In_2O_{3-x} catalyst. *ACS Catal.* **10**, 11307–11317 (2020).
58. K. Chen, H. Fang, S. Wu, X. Liu, J. Zheng, S. Zhou, X. Duan, Y. Zhuang, S. Chi Edman Tsang, Y. Yuan, CO_2 hydrogenation to methanol over Cu catalysts supported on La-modified SBA-15: The crucial role of Cu–LaO_x interfaces. *Appl. Catal. B* **251**, 119–129 (2019).
59. Q. Tan, Z. Shi, D. Wu, CO_2 hydrogenation to methanol over a highly active Cu–Ni/CeO_2–nanotube catalyst. *Ind. Eng. Chem. Res.* **57**, 10148–10158 (2018).

Acknowledgments: We appreciate R. Prins (ETH Zurich) for helpful discussions. **Funding:** This work was supported by a Key Basic Research Project (18JC1412100) from the Shanghai Municipal Science and Technology Commission, the National Natural Science Foundation of China (22072043, 21773069, 21703137, 21703069, and 21473057), and the National Key Basic Research Program (2011CB201403) of the Ministry of Science and Technology of the People's Republic of China. **Author contributions:** Y. Lu and G.Z. conceived the idea for the project. C.M. and P.C. conducted material synthesis. C.M. performed structural characterizations and catalytic test. X.-R.S. performed DFT calculations. Y. Lu, G.Z., C.M., X.-R.S., and Y. Liu analyzed the catalytic results. C.M., G.Z., X.-R.S., and Y. Lu drafted the manuscript. Y. Lu directed the research. All authors discussed and commented on the manuscript. **Competing interests:** Y. Lu, P.C., G.Z., and Y. Liu have a patent application related to this work filed with the Chinese Patent Office on 15 October 2017 (201710956080.1). The authors declare no other competing interests. **Data and materials availability:** All data needed to evaluate the conclusions in the paper are present in the paper and/or the Supplementary Materials.

Submitted 19 March 2021
Accepted 17 June 2021
Published 4 August 2021
10.1126/sciadv.abi6012

Citation: C. Meng, G. Zhao, X.-R. Shi, P. Chen, Y. Liu, Y. Lu, Oxygen-deficient metal oxides supported nano-intermetallic $InNi_3C_{0.5}$ toward efficient CO_2 hydrogenation to methanol. *Sci. Adv.* **7**, eabi6012 (2021).